1 **Revision 1**

2 **Harmunite CaFe$_2$O$_4$ – a new mineral from the Jabel Harmun, West Bank, Palestinian**

3 **Autonomy, Israel**

4

5 IRINA O. GALUSKINA[1], YEVGENY VAPNIK[2], BILJANA LAZIC[3], THOMAS ARMBRUSTER[3],

6 MIKHAIL MURASHKO[4], EVGENY V. GALUSKIN[1]

7

8 [1]Faculty of Earth Sciences, Department of Geochemistry, Mineralogy and Petrography,

9 University of Silesia, Będzińska 60, 41-200 Sosnowiec, Poland

10 *corresponding author, e-mail: irina.galuskina@us.edu.pl

11 [2]Department of Geological and Environmental Sciences, Ben-Gurion University of the

12 Negev, P.O.B. 653, Beer-Sheva 84105, Israel

13 [3] Mineralogical Crystallography, Institute of Geological Sciences, University of Bern,

14 Freiestr. 3, CH-3012 Bern, Switzerland

15 [4]Systematic Mineralogy, 44, 11$^{th}$ line V.O, apt. 76, Saint-Petersburg 199178, Russia

16

17 **ABSTRACT**

18     Harmunite, naturally occurring calcium ferrite CaFe$_2$O$_4$, was discovered in the

19 Hatrurim Complex of pyrometamorphic larnite rocks close to the Jabel Harmun, the Judean

20 Desert, West Bank, Palestinian Autonomy, Israel. The new mineral occurs in pebbles of the

21 pseudo-conglomerate consisting of intensely altered larnite-bearing rocks. Srebrodolskite,

22 magnesioferrite and harmunite are intergrown forming black porous aggregates to the central

23 part of the pebbles. Larnite, fluorellestadite, ye'elimite, fluormayenite, gehlenite, ternesite and

24 calciolangbeinite are the main associated minerals. Empirical crystal chemical formula of

25 harmunite from type specimen is as follows

1

26    $Ca_{1.013}(Fe^{3+}_{1.957}Al_{0.015}Cr^{3+}_{0.011}Ti^{4+}_{0.004}Mg_{0.003})_{\Sigma1.993}O_4$. Calculated density is 4.404 g/cm$^3$,

27    microhardness VHN$_{50}$ is 655 kg/mm$^2$. The Raman spectrum of harmunite is similar to that of

28    the synthetic analogue. Harmunite in hand specimen is black and under reflected plane

29    polarized light is light grey with red internal reflections. Reflectance data for the COM

30    wavelengths vary  from ~22% (400 nm) to ~18% (700 nm).

31         The crystal structure of harmunite (*Pnma*; $a = 9.2183(3)$ Å, $b = 3.0175(1)$ Å, $c =$

32    10.6934(4) Å; $Z = 4$, $V = 297.45(2)$ Å$^3$), analogous to the synthetic counterpart, was refined

33    from X-ray single-crystal data to $R1 = 0.0262$. The structure of CaFe$_2$O$_4$ consist of two

34    symmetrically independent FeO$_6$ octahedra connected over common edges, forming double

35    rutile-type $^1_\infty$[Fe$_2$O$_6$] chains. Four such double chains are further linked by common oxygen

36    corners creating a tunnel-structure with large trigonal prismatic cavities occupied by Ca along

37    [001]. The strongest diffraction lines are as follows ($d_{hkl}$, $I$): 2.6632 (100), 2.5244 (60), 2.6697

38    (52), 1.8335 (40), 2.5225 (35), 2.2318 (34), 1.8307 (27), 1.5098 (19).

39         Crystallization of harmunite takes place in the presence of sulphate melt.

40

41

42    Key words: harmunite, calcium ferrite, Raman, structure, Jabel Harmun, Palestinian

43    Autonomy, Israel

44

45

46

47

48

49

50

51

**INTRODUCTION**

53    The new mineral harmunite $CaFe_2O_4$ (IMA2012-045) was discovered in

54    pyrometamorphic larnite rocks belonging to the Hatrurim Formation (also known as the

55    "Mottled Zone"; Bentor 1960; Gross 1977; Vapnik et al. 2007; Novikov et al. 2013). The

56    name is given after Mt. Harmun (Jabel Harmun in Arabic language) where the rock was

57    sampled, at the Hatrurim Formation complex situated in the Judean Desert, West Bank,

58    Palestinian Autonomy, Israel (31°46′ N - 35°26′ E). Type materials were deposited in the

59    mineralogical collections of the Saint Petersburg University, Russia, catalogue number

60    1/19518, and of the Fersman Mineralogical Museum, Moscow, Russia, catalogue number

61    4398/1.

62    Natural $CaFe_2O_4$ was previously described from burned fossilized woody relics of

63    siderite composition enclosed in pyrogenic iron ore in an ancient fire of the Kuzbass, Russia

64    (Nigmatulina and Nigmatulina 2009). This mineral, which the authors called "aciculite", has a

65    significant Mn content (4.64-6.70 wt.% MnO) and forms exsolution structures in

66    magnesioferrite (Nigmatulina and Nigmatulina 2009). Furthermore, $CaFe_2O_4$ also named

67    "aciculite", was described from a burnt damp of the Chelyabinsk coal basin by Chesnokov et

68    al. (1998). The origin of this phase is considered as anthropogenic; therefore it was not

69    approved by the CNMNC of the IMA as a valid mineral species.

70    Synthetic calcium ferrite, $CaFe_2O_4$ is a well known material widely used as a pigment,

71    catalyzer, thermally-stable material, conductor, solid electrolyte, ceramic material etc.

72    (Candeia et al. 2004; Kharton et al. 2008). Its crystal structure was first reported by Hill et al.

73    (1956) and then by Decker and Kasper (1957).

74    Many isotypic compounds have been reported and "calcium-ferrite type" became the

75    common term used for structural description. For instance, Shizuya et al. (2007) has

3

76    summarized related compounds having the $CaFe_2O_4$ structure type, based on the $AB_2O_4$

77    chemical formula (A = Li, Na, Mg, Ca, Sr, Ba, La, and Eu; B = Ti, V, Cr, Mn, Fe, Ru, Rh, Al,

78    Ga, In, Tl, Sc, Y, La, Pr, Nd, Sm, Eu, Gd, Tb, Dy, Ho, Yb, and Lu). In nature only two phases

79    possessing this structure type are known: xieite $FeCr_2O_4$ (*Bbmm*, *a* = 9.462(6) Å, *b* = 9.562(9)

80    Å, *c* = 2.916(1) Å) – high-pressure polymorph of chromite (Chen et al. 2008), and marokite

81    $CaMn_2O_4$ (*Pmab* or *P21ab*, *a* = 9.71(2) Å, *b* = 10.03(2) Å, *c* = 3.162(5) Å) – low-pressure

82    phase (Gaudefroy et al. 1963; Lepicard and Protas 1966).

83          The $CaFe_2O_4$ (**CF**) structure type, including the two slightly distorted modifications

84    $CaTi_2O_4$ (**CT**) and $CaMn_2O_4$ (**CM**) became interesting for the geoscience community, when

85    they were proposed as high-pressure form of spinels (Irifune et al. 1991; Kirby et al. 1996). At

86    the P, T - conditions of the mantle transition zone the spinel structure is no longer stable and it

87    is expected to transform to the calcium-ferrite type. Thus this structure type is considered as

88    "potential geochemical reservoir in the mantle for alkaline and other large cations" (Merlini et

89    al. 2010).

90          In the present paper we report results on the properties and mineral association of

91    harmunite from the Hatrurim Complex. In addition, we use the opportunity to provide better

92    quality structure data obtained from single-crystal X-ray analysis than the original data

93    reported by Hill et al. (1956).

94

95    **GEOLOGAL SETTING**

96          The Jabel Harmun is one of several pyrometamorphic complexes of the Hatrurim

97    Formation located in the Judean Desert in the vicinity of the Jerusalem-Jericho highway (Fig.

98    1; Khesin et al. 2010a, b; Sokol et al. 2010, 2011, 2012; Seryotkin  et al. 2012; Novikov et al.

99    2013). Hilly landscape of the Hatrurim Formation is characterized by the differently colored

100   outcrops of rocks (Fig. 2), consisting of high- and ultra-high temperature calcium-silicate, -

4

101  aluminate and –ferrite minerals embedded in a low-temperature hydrated calcium silicate

102  matrix (Fig. 3). Formation of paralava suggests that the pyrometamorphic process was locally

103  intense causing partial or bulk melting of the rocks. The rock complexes do not preserve any

104  sedimentary features and are extremely brecciated, showing numerous genetically different

105  types of breccias.

106       The origin of pyrometamorphic rocks of the Hatrurim Formation found on the territory

107  of Israel, Palestinian Autonomy and Jordan, remains disputable (Matthews and Gross 1980;

108  Sokol et al. 2010, 2012; Geller et al. 2012; Kolodny et al. 2013; Vapnik and Novikov 2013).

109  Most researchers adopt the point of view that fires causing pyrometamorphism were induced

110  by combustion of bituminous chalk containing carbon $C_{org.}$ content up to 15 wt.% in the

111  Negev (Minster et al. 1997) and up to 22 wt.% in the Nabi Musa (Picard 1931) of the Ghareb

112  Formation (Maastrichtian) (Gur et al. 1995; Burg et al. 1991, 1999). According to this model,

113  combustion occurred in the time space from 16 Ma to 200 Ka (Gur et al. 1995; Porat et al.

114  1991). Such a model encounters numerous problems (Novikov et al. 2013). For example,

115  geological observations indicate that the stratigraphic position of the Hatrurim Formation is

116  different than that of the Ghareb Formation, e.g., pyrometamorphic complexes of the

117  Hatrurim Formation may occur above, below and/or in the same horizon as the Ghareb

118  Formation (Vapnik and Novikov 2013; Novikov et al. 2013). The term "Hatrurim Formation"

119  has stratigraphic implication and has been erroneously applied in the past to those

120  pyrometamorphic rocks. Therefore, we prefer to use the term "Hatrurim Complex".

121       Recently, the origin of the Hatrurim Complex was connected to neotectonic activity in

122  the vicinity of the Dead Sea Transform Fault.  Anomalously high pressures were noted within

123  the deep sedimentary layers and led to hydrothermal flows of hydrocarbon gas and fluidized

124  matter. Such process is described as mud volcanism (Kopf 2002). The spontaneous

5

125    combustion of hydrocarbons near the surface is a known phenomenon related to modern mud

126    volcanoes (Kovalevskiy 1940; Shnyukov et al. 1978; Fishman et al. 2012).

127    The major features supporting at least partial influence of the mud volcanism for the Hatrurim

128    Complex genesis are: 1) the existence of feeder channels and clastic dikes, rich in quartz sand

129    and filled by breccias, composed of fragments of sedimentary and pyrometamorphic rocks

130    (Vapnik and Sokol 2006; Vapnik and Novikov 2013); 2) the existence of several outcrops of

131    the Hatrurim Formation on the slopes of modern wadies (Vapnik and Novikov 2013).

132        Jabel Harmun pyrometamorphic complex is composed of spurrite- and larnite-bearing

133    rocks, and overlies the phosphorite, carbonate, and chert layers of the Mishash Formation

134    (Campanian). Jabel Harmun rocks grades laterally into bituminous and non-bituminous chalk of

135    the Ghareb Formation (Maastrichtian) (Soudry 1973). Bituminous series show the maximum

136    thickness of 40 m and overlain by 10-30 m of non-bituminous chalk. The maximal thickness of

137    the Jabel Harmun complex is 90-100 m (Novikov et al. 2013). The rocks of the Jabel Harmun

138    complex are also located as isolated foci within non-bituminous chalk of the Ghareb Formation

139    (Fig. 2). High-temperature rocks are commonly altered and hosted by low-temperature

140    hydrothermal hydrated calcium silicate rocks, often enriched in secondary carbonates. It seems

141    that larnite-bearing rocks are most intensely subjected to low-temperature alteration, resulting in

142    the formation of larnite nodules or pseudo-conglomerates (the local term; Gross 1977),

143    occasionally included in the low-temperature hydrothermal matrix (Fig. 3) and/or form loose

144    deposits. A few outcrops of gehlenite-bearing rock were also found. In several cases such rock

145    shows amygdular texture, suggesting at least partial melting of the original rocks.

146

147    **METHODS OF INVESTIGATIONS**

148        Crystal morphology and chemical composition of harmunite and associated minerals

149    were examined using optical microscopes, analytical electron scanning microscope (Philips

6

150  XL30 ESEM/EDAX, Faculty of Earth Sciences, University of Silesia) and electron probe

151  microanalyzer (CAMECA SX100, Institute of Geochemistry, Mineralogy and Petrology,

152  University of Warsaw). Electron probe microanalyses of harmunite were performed at 15 kV

153  and 20 nA using the following lines and standards: Ca$K\alpha$, Si$K\alpha$ – wollastonite; Al$K\alpha$ –

154  orthoclase; Cr$K\alpha$ – $Cr_2O_3$;  Fe$K\alpha$ – hematite; Mn$K\alpha$ – rhodochrosite; Ti$K\alpha$ – rutile; Mg$K\alpha$ –

155  diopside; Na$K\alpha$ – albite.

156      The Raman spectra of harmunite were recorded using a WITec confocal CRM alpha

157  300 Raman microscope (Jagiellonian Centre for Experimental Therapeutics, Cracow)

158  equipped with an air-cooled solid-state laser operating at 488 nm and a CCD detector which

159  was cooled to -82 ºC. The laser was coupled to the microscope via a single mode optical fiber

160  with a diameter of 50 µm. An Olympus MPLAN (1006/0.90NA) objective was used. The

161  scattered radiation was focused onto a multi-mode fiber (50 µm diameter) and

162  monochromator. The power of the laser at the sample position was 44 mW for measurement.

163  One hundred fifty scans with integration times of 0.3-0.5 s and a resolution of 3 cm$^{-1}$ were

164  collected and averaged. The monochromator of the spectrometer was calibrated using the

165  Raman scattering line produced by a silicon plate (520.7 cm$^{-1}$).

166      Single-crystal X-ray study of harmunite was carried out using a Bruker APEX II

167  SMART diffractometer, Mo$K\alpha$, $\lambda = 0.71073$ Å, (Institute of Geological Sciences, University

168  of Bern). Diffraction data were collected with ω scans at different φ settings (φ-ω scan)

169  (Bruker 1999). Data were processed using SAINT (Bruker 2011). An empirical absorption

170  correction using SADABS (Bruker 2011) was applied. The harmunite structure was refined

171  using neutral atom scattering factors with the program SHELX97 (Sheldrick 2008) to $R_1 =$

172  2.6%.

173      X-ray powder diffraction data were collected using an X'Pert PRO 3040/60

174  diffractometer  (Cu$K\alpha$, $\lambda = 1.540598$ Å), Theta-Theta geometry (Faculty of Earth Sciences,

7

175    University of Silesia). PANalytical HighScore+ software, using the ICDD PDF 4+ database

176    version 2011, were used for interpretation and Rietveld refinement. Structural parameters of

177    synthetic $CaFe_2O_4$ (PDF 04-007-8642, Decker and Kasper 1957) were used as starting

178    structural model of harmunite.

179         Reflectance data  of harmunite measured using a Zeiss 521 VIS microscope for

180    standard wavelengths are as following (max/min %):   470 nm 21.60/20.10, 546 nm

181    20.65/19.20, 589 nm 19.30/18.45, 650 nm 18.70/17.75 (Standard Zeiss SiC reflectance

182    standard, number 472, 20% Refl.).

183

184    **OCCURENCE AND PARAGENESIS**

185         The occurrence of harmunite is restricted to pebbles of a pseudo-conglomerate

186    collected on the southern slope of the Jabel Harmun. Srebrodolskite $Ca_2Fe_2O_5$,

187    magnesioferrite $MgFe_2O_4$ and harmunite form together black porous aggregates in the central

188    part of these pebbles (Fig. 3A-C). Besides larnite $\beta$-$Ca_2SiO_4$, fluorellestadite

189    $Ca_5(SiO_4)_{1.5}(SO_4)_{1.5}F$, ye'elimite $Ca_4Al_6(SO_4)O_{12}$, fluormayenite $Ca_{12}Al_{14}O_{32}F_2$ (IMA2013-

190    019, Galuskin et al. 2013) , gehlenite $Ca_2Al_2SiO_7$, and ternesite $Ca_5(SiO_4)SO_4$ are the main

191    associated minerals. Minor and accessory minerals are magnesioferrite, minerals of the

192    srebrodolskite-brownmillerite series $Ca_2Fe^{3+}_2O_5$- $Ca_2Fe^{3+}AlO_5$, Si-bearing perovskite, and

193    barite. Vorlanite $CaUO_4$ (Galuskin et al. 2011), recently discovered nabimusaite

194    $KCa_{12}(SiO_4)_4(SO_4)_2O_2F$ (Galuskin et al. 2013), shulamitite $Ca_3TiFeAlO_8$ (Sharygin et al.

195    2013) and vapnikite $Ca_3UO_6$ (IMA2013-082, Galuskin et al. 2013) and the potentially new

196    mineral $CaCu_2S_2$, are rarely noted. Ternesite was discovered from xenoliths in volcanites of

197    Eifel, Germany (Irran et al. 1997), the Jabel Harmun locality is the second natural finding.

198    Ternesite from the Jabel Harmun locality is characterized by high phosphorus content (up to 6

199    wt.% $P_2O_5$) and forms poikiloblasts up to 5 mm in size in the dark-brown parts of the pebble

8

200    (Fig. 3A). Less frequently it forms light-green spherules 3-4 mm in diameter  irregularly

201    distributed in larnite rocks.

202         Light colored aggregates of hydrated Ca, K and Na sulphates (Fig. 4B) became

203    obvious around black ore minerals after the sample was rinsed with water. We were able to

204    identify the following sulphates: calciolangbeinite $K_2Ca_2(SO_4)_3$, aphthitalite $K_3Na(SO_4)_2$ and

205    thenardite $Na_2SO_4$. Thenardite forms decomposition structures in aphthitalite and occurs on

206    fresh surfaces within porous aggregates of ore minerals (Fig. 5A, 6). Calciolangbeinite has a

207    composition according to the ideal crystal-chemical formula $K_2Ca_2(SO_4)_3$. This is in contrast

208    to holotype calciolangbeinite,which has a significant Mg content, recently discovered in the

209    Yadovitaya fumarole, Tolbachik volcano, Kamchatka Oblast', Far-Eastern Region, Russia

210    (Pekov et al. 2012). Calciolangbeinite with inclusions of relatively large crystals (up to 100

211    µm) of magnesioferrite and fluorellestadite sometimes fill short cracks about 1 mm in

212    thickness, in larnite rocks. Aphthitalite with relics of thenardite occurs as amoeboidal

213    aggregates in calciolangbeinite (Fig. 6). Even if aphthitalite is partially dissolved, it may be

214    assumed that calciolangbeinite and aphthitalite (+thenardite) formed as a result of

215    simultaneous crystallization from a sulphate-bearing liquid phase or decomposition of a

216    complex sulphate solid solution. Barite and fluorellestadite are noted at the boundary of Ca-K

217    and Na-K sulphates (Fig. 6).

218         At the margins of ore aggregates magnesioferrite with admixture of srebrodolskite is

219    predominant (Fig. 5A), whereas at the central part of the aggregates harmunite and

220    srebrodolskite are prevail (Fig. 4C). In porous ore aggregates, partially filled by Ca-, K-, Na-

221    sulphates, well-formed crystals of fluorellestadite (Fig. 5B), larnite, native copper and

222    umangite $Cu_3Se_2$ (Fig. 5A, C) and also native silver (Fig. 5C) are observed.

223

9

224 **HARMUNITE: PHYSICAL PROPERTIES, CHEMICAL COMPOSITION AND**

225 **RAMAN SPECTRA**

226 Aggregates of harmunite, srebrodolskite and magnesioferrite have skeletal structure

227 (Fig. 4C, 5A). Parallel aggregates of prismatic orthorhombic harmunite crystals reach 2-3 mm

228 in size. Twinning of harmunite is not observed. Harmunite crystals are bounded by faces of

229 the {100}, {110}, {210}, {011}, {001}, and {010} forms, but also occur as rounded

230 fragments (Fig. 3C). Rounded crystals were also recognized for srebrodolskite and

231 magnesioferrite. This phenomenon, known as antiskeletal growth (Punin and Franke 2004), is

232 well displayed on octahedral crystals of magnesioferrite with minor {001} and {110} faces

233 (Fig. 5B).

234 Macroscopically harmunite is black. In reflected light it is light grey with internal red

235 reflections (Fig. 4E, F; 7). Reflectance intensity of harmunite decreases with wavelength from

236 ~22% (400 nm) to ~18% (700 nm) (Table 1, supplementary materials). The measured

237 microhardness is $VHN_{50} = 655$ kg mm$^{-2}$ (mean of 10 measurements), range 540-700 kg mm$^{-2}$;

238 equivalent to a Mohs hardness of ~5½. It was not possible to measure the density of

239 harmunite due to the high porosity of its aggregates. The calculated density is 4.404 g/cm$^3$

240 using the empirical formula (Table 2, analysis 1).

241 Harmunite was also found in pebbles of greenish larnite rock (pseudo-conglomerate)

242 collected a few tens of meters away from the original locality of harmunite. Here it forms

243 exsolution-like structures in magnesioferrite (Fig. 8). The composition of this rock is

244 approximately the same as for the holotype specimen containing harmunite. However, the

245 main difference is the absence of ternesite and fluorellestadite, instead of which fluorapatite

246 with high Si and S contents appears. The rock riches in spinel, brownmillerite-srebrodolskite,

247 and shulamitite (up to 15% of the total volume). Spinel composition varies from ferrian spinel

248 to magnesioferrite.

10

249      Composition of holotype harmunite is close to the composition of the end-member

250   $CaFe_2O_4$ (Table 2). Increased impurities of Mn, Cr and Al are characteristic for harmunite of

251   exsolution-like structures in magnesioferrite. Impurity of manganese in holotype harmunite is

252   below the detection limit of EPMA (Table 2).

253      The Raman spectrum of holotype harmunite (Fig. 9) corresponds to the spectrum of

254   synthetic ferrite $CaFe_2O_4$, for which 42 Raman modes are active (Kolev et al. 2003). The

255   main Raman bands of harmunite are follows (cm$^{-1}$): 1228 [combination first-order phonons $A_g$

256   (648) + $A_g$ (585)]; 648 ($A_g$); 585 ($A_g$); 519 ($B_{2g}$); 453 and 435 ($A_g$); 379 and 364 ($A_g/B_{1g}/B_{3g}$);

257   298 ($A_g$); 270 ($A_g$); 206 ($A_g$); 182 ($A_{g/}B_{2g}$); 117 ($A_g$). The Raman spectrum of harmunite from

258   exsolutions in magnesioferrite is very similar to that of one of holotype harmunite.  The main

259   difference is a strong band at 344 cm$^{-1}$ ($A_g/B_{1g}/B_{3g}$) on the spectrum of harmunite from

260   exsolutions in magnesioferrite reported for zz Raman scattering configurations of synthetic

261   $CaFe_2O_4$ (Kolev et al. 2003).

262

263   **CRYSTALLOGRAPHY**

264      X-ray powder-diffraction data (in Å for Cu$K\alpha$) are listed in Table 3. Unit cell

265   parameters refined from the powder data are: *Pnma, a* = 9.2179(2), *b* = 3.0180(9), *c* =

266   10.6929(2) Å, *V* = 297.47(1) Å$^3$, *Z* = 4.

267      The crystal structure of harmunite (*Pnma*; *a* = 9.2183(3) Å, *b* = 3.0175(1) Å, *c* =

268   10.6934(4) Å; *V* = 297.45(2) Å$^3$) was refined from X-ray single-crystal data to *R*1 = 0.0262.

269   Details of data collection and structure refinement are given in Table 4, final atomic

270   coordinates are summarized in Table 5. Selected bond lengths are listed in Table 6. The

271   structure corresponds to that of synthetic $CaFe_2O_4$ (Decker and Kasper 1957; Yamanaka et al.

272   2008; Merlini et al. 2010). The structure of $CaFe_2O_4$ consist of two symmetrically

273   independent $FeO_6$ octahedra connected over common edges, forming double rutile-type

11

274   $_\infty^1[Fe_2O_6]$ chains. Four such double chains are further linked by common oxygen corners

275   creating a tunnel-structure with large trigonal prismatic cavities along [001] (Fig.10). These

276   cavities are occupied by Ca-cations. Ca atoms have six shorter bonds (trigonal prism) and two

277   longer bonds to oxygen atoms (Table 6, Fig. 10).

278

279   **DISCUSSION**

280         After marokite $CaMn_2O_4$ (Gaudefroy et al. 1963), harmunite $CaFe_2O_4$ is the second

281   "calcium ferrite" structure type mineral forming at low pressure. Analysis of the bond-valence

282   sums (bvs) (Brown and Altermatt 1985) in harmunite and marokite shows that Ca-atoms are

283   squeezed into structural tunnels. Typical signs for this compression are the overbonding of the

284   Ca –atom with bvs(Ca) = 2.259 v.u. for harmunite and bvs(Ca) = 2.263 v.u. for marokite

285   (Table 7) as well as underbonding of the two octahedral sites (bvs(Fe1) = 2.795(6) and

286   bvs(Fe2) =  2.832(6) v.u. in harmunite and bvs(Mn) = 2.886(14) for both octahedra in

287   marokite). This tendency is also observed for the high pressure phases of $CaAl_2O_4$ (Lazic et

288   al. 2006) and $CaGa_2O_4$ (Lazic et al. 2005), showing even more pronounced bond-sums

289   deviations, as expected from high pressure structures. A few similar examples are listed in

290   Table 7.  For all compounds, the global instability index (GII) was calculated (Salinas-

291   Sánchez et al. 1992) at different P-  and T- conditions. The GII gives a numerical value for

292   overall structure stability, comparing the calculated bond-valence sums with ideal values.

293   According to Brown (2002), a GII larger than 0.20 v.u., indicates a structure so strained to be

294   unstable, the usual case for structures synthesized under extreme conditions (Table 7).

295         The rarity of Ca-ferrites in nature can be explained by their high formation

296   temperature. Data on the synthesis and stability of synthetic $CaFe_2O_4$ and $Ca_2Fe_2O_5$, and also

297   the known conditions of cement clinker production, suggest that crystallization of these

298   ferrites begins above 700 °C (Candeia at al. 2004, Žáček et al. 2005). $CaFe_2O_4$ and $Ca_2Fe_2O_5$

12

299  are stable at atmospheric pressure up to 1216 °C   and 1449 °C, respectively (Forsbers et al.

300  2002).

301      The size of harmunite, srebrodolskite and magnesioferrite crystals in ore aggregates

302  and in rare cracks filled by K-, Ca-, Na-sulphates is two orders of magnitude greater than the

303  size of srebrodolskite-brownmillerite and magnesioferrite grains in larnite rock formed as a

304  result of solid-phase reactions. It may be assumed that a small amount of sulphate melt, filling

305  small pores in larnite rock, formed as a result of protolith clinkerisation. Appearance of

306  intergranular sulphate melts is well known in industrial production of clinker with high

307  gypsum content (Taylor 1997). Growth of relatively large ferrite crystals took place with the

308  participation of sulphate melt, which later solidified as calciolangbeinite and aphthitalite (Fig.

309  6). The angular form of ore aggregates containing harmunite (Fig. 4B) suggests primary

310  fragments of sedimentary rock enriched in iron. As a result of pyrometamorphic processes the

311  original Fe minerals were replaced by aggregates of srebrodolskite and harmunite. The

312  protolith was also a source of Mg leading to magnesioferrite enrichment in the marginal zone

313  of these aggregates and occurrence of individual magnesioferrite crystals in the core. The

314  melting point of calciolangbeinite is just above 1000 °C (Taylor 1997). However, we are

315  unable to reconstruct the detailed composition of this sulphate melt (probably, sulphate-

316  chloride with cations like Na, K, Ca, Fe, Ba...). Thus the melt temperature could have been

317  significantly lower. It may be assumed that locally elevated Fe inside an ore aggregate leads

318  to the reaction of sulphates with early srebrodolskite: $Fe_2(SO_4)_3 + Ca_2Fe_2O_5 = 2CaFe_2O_4 +$

319  $3SO_3$. This sulphate melt was probably the sulfur source for the subsequent formation of

320  relatively large poikiloblasts such as ternesite and fluorellestadite.

13

330    **REFERENCES**

331    Andrault, D. and Bolfan Casanova, N. (2001) High-pressure phase transformations in the

332        $MgFe_2O_4$ and $(Fe_2O_3)$-$(MgSiO_3)$ systems. Physics and Chemistry of Minerals, 28, 211-217.

333    Bentor, Y.K. (ed.) (1960) Israel. In: Lexique Stratigraphique International, Vol. III, Part 10.2,

334        Asie. 80 p., Paris.

335    Brown, I.D. (2002) The Chemical Bond in Inorganic Chemistry. The Bond Valence Model,

336        International union of Crystallography Monographs on Crystallography, vol. 12, Oxford

337        Univ. Press, Oxford, UK.

338    Brown, I.D. and Altermatt, D. (1985) Bond-valence parameters obtained from a systematic

339        analysis of the Inorganic Crystal Structure Database. Acta Crystallographica, B41, 244-247.

340    Bruker (2011) SAINT, SADABS. Bruker AXS Inc., Madison,Wisconsin, USA.
341
342    Burg, A., Kolodny, Y., and Lyakhovsky, V. (1999) Hatrurim-2000: The "Mottled Zone"

343        revisited, forty years later. Israel Journal of Earth Sciences, 48, 209-223.

344    Burg, A., Starinsky, A., Bartov, Y., and Kolodny, Y. (1991) Geology of the Hatrurim Formation

345        ("Mottled Zone") in the Hatrurim basin. Israel Journal of Earth Sciences, 40, 107-124.

346    Candeia, R.A., Bernardi, M.I.B., Longo, E., Santos, I.M.G., and Souza, A.G. (2004) Synthesis

347        and characterization of spinel pigment $CaFe_2O_4$ obtained by the polymeric precursor

348        method. Materials Letters, 58, 569-572.

349    Chen, M., Shu J., and Mao, H. (2008) Xieite, a new mineral of high-pressure $FeCr_2O_4$

350        polymorph. Chinese Science Bulletin, 53, 3341-3345.

14

351     Chesnokov, B., Kotrly, M., and Nisanbajev, T. (1998) Brennende Abraumhalden und

352        Aufschlüsse im Tscheljabinsker Kohlenbecken - eine reiche Mineralienküche.

353        Mineralien-Welt, 9(3), 54-63.

354     Decker, B.F. and Kasper, J.S. (1957) The structure of calcium ferrite. Acta Crystallographica,

355        10, 332-337.

356     Fishman, I.L., Kazakova, Yu.I., Sokol, E.V., Stracher, G.B., Kokh, S.N., Polyansky, O.P.,

357        Vapnik, Ye., White, Ye., and Bajadilov, K.O. (2012) Mud volcanism and gas combustion

358        in the Yli Depression, Southeastern Kazakhstan. In: Coal and Peat Fires: A global

359        perspective. Vol. 2: Photographs and Multimedia Tours (Ed. by G.B. Stracher, A.

360        Prakash, and E.V. Sokol) 215-229 p., Elsevier.

361     Forsbers, S., Wikström, P., and Rosén, E. (2002) Determination of Gibbs energies of

362        formation of $CaFe_2O_4$ and $Ca_2Fe_2O_5$ from solid-state EMF measurements using $CaF_2$ as

363        solid electrolyte. Metallurgical and Materials Transactions B, 33b, 385-391.

364     Galuskin, E.V., Armbruster, T., Galuskina, I.O., Lazic, B., Winiarski, A., Gazeev, V.M.,

365        Dzierżanowski, P., Zadov, A.E., Pertsev, N.N., Wrzalik, R., Gurbanov, A.G., and

366        Janeczek, J. (2011) Vorlanite $(CaU^{6+})O_4$ – A new mineral from the Upper Chegem

367        caldera, Kabardino-Balkaria, Northern Caucasus, Russia. American Mineralogist, 96,

368        188-196.

369     Galuskin, E.V., Galuskina, I.O., Kusz, J., Armbruster, T., Marzec, K., Dzierżanowski, P., and

370        Murashko, M. (2013) Vapnikite, IMA2013-082. CNMNC Newsletter No. X, Month

371        2013, page X; Mineralogical Magazine, XX, XXX-XXX.

372     Galuskin, E.V., Gfeller, F., Armbruster, T., Galuskina, I.O., Vapnik, Ye., Murashko, M. and

373        Dzierżanowski, P. (2013) Fluormayenite, IMA 2013-019. CNMNC Newsletter No. 16,

374        August 2013, page 2705; Mineralogical Magazine, 77, 2695-2709.

15

375   Galuskin, E.V., Gfeller, F., Armbruster, T., Galuskina, I.O., Vapnik,Ye., Murashko, M.,

376        Włodyka, R., and Dzierżanowski, P. (2013) Nabimusaite, IMA2011-112. CNMNC

377        Newsletter No. 15, February 2013, page 5; Mineralogical Magazine, 77, 1-12.

378   Gaudefroy, C., Jouravsky, G. and Permingeat, F. (1963) La marokite, $CaMn_2O_4$ une nouvelle

379        éspèce minérale. Bulletin de la Société Française de Minéralogie et de Cristallographie,

380        86, 359-67.

381   Geller, Y.I., Burg, A., Halicz, L., and Kolodny, Y. (2012) System closure during the

382        combustion metamorphic ”Mottled Zone” event, Israel. Chemical Geology, 334, 25-36.

383   Gross, S. (1977): The mineralogy of the Hatrurim Formation, Israel. Geological Survey of

384        Israel Bulletin, 70 p.

385   Gur, D., Steinitz, G., Kolodny, Y., Starinsky, A., and McWilliams, M. (1995) $^{40}Ar/^{39}Ar$ dating

386        of combustion metamorphism (“Mottled Zone”, Israel). Chemical Geology, 122, 171–

387        184.

388   Hill, P.M., Peiser, H.S., and Rait, J.R.  (1956) The crystal structure of calcium ferrite and β-

389        calcium chromite, Acta Crystallographica, 9, 981-986.

390   Horyń, R. and Lukaszewicz, K. (1966) Refinement of the Crystal Structure of $CaCs_2O_4$,

391        Bulletin de l'Academie Polonaise des Sciences, Serie des Sciences Chimiques, 14, 499-

392        504.

393   Hörkner, W. and Müller-Buschbaum, H. (1976) Einkristalluntersuchung von β-$CaCr_2O_4$,

394        Zeitschrift fuer Naturforschung, Teil B. Anorganische Chemie, Organische Chemie, 31,

395        1710-1711.

396   Irifune, T., Fujino, K., and Ohtani, K. (1991) A new high pressure form of $MgAl_2O_4$. Nature,

397        349, 409-411.

398   Irran, E., Tillmanns, E., and Hentschel, G. (1997) Ternesite, $Ca_5(SiO_4)_2SO_4$, a new mineral

399        from the Ettringer Bellerberg, Eifel, Germany. Mineralogy and Petrology, 60, 121-132.

16

400    Kharton, V.V. , Tsipis, E.V., Kolotygin, V.A., Avdeev, M., Viskup, A.P., Waerenborgh,

401        J.C., and Frade, J.R. (2008) Mixed conductivity and stability of $CaFe_2O_4$-$\delta$. Journal of the

402        Electrochemical Society, 155, 3, 13-20.

403    Khesin, B., Vapnik, Ye., and Itkis, S. (2010a) Geophysical evidence of deep hydrocarbon flow in

404        Mottled Zone areas, Dead Sea Transform zone. Geophysics, 75, B91-B101.

405    Khesin, B., Vapnik, Ye., and Itkis, S. (2010b) Unconventional view of hydrocarbon prospecting in

406        Israel and adjacent areas. First Break, 28, 103-109.

407    Kirby, S.H., Stein, S., Okai, E.A., and Rubie, D.C. (1996) Metastable mantle phase transformations

408        and deep earthquakes in subducting oceanic lithosphere. Review of Geophysics, 34, 261–306.

409    Kojitani, H., Hisatomi, R., and Akaogi, M. (2007) High-pressure phase relations and crystal

410        chemistry of calcium ferrite-type solid solutions in the system $(MgAl_2O_4)$-$(Mg_2SiO_4)$. American

411        Mineralogist, 92, 1112-1118.

412    Kolev, N., Iliev, M.N., Popov, V.N., and Gospodinov, M. (2003) Temperature-dependent

413        polarized Raman spectra of $CaFe_2O_4$. Solid State Communications, 128, 153-155.

414    Kolodny, Y., Burg, A., and A. Sneh, A. (2013) Comment on Combustion metamorphism

415        (CM) in the Nabi Musa dome: new implications for a mud volcanic origin of the Mottled

416        Zone, Dead Sea area by: E. Sokol, I. Novikov, S. Zateeva, Ye.Vapnik, R. Shagam and O.

417        Kozmenko, Basin Research (2010) 22, 414–438. Basin Research, 25 (1), 112 – 114.

418    Kopf, A.J. (2002) Significance of Mud Volcanism. Review in Geophysics, 40, 1005-1057.

419    Kovalevskiy, S.A. (1940) Mud volcanoes of the southern Caspian (Azerbaijan and Turkmenia).

420        200 p., Azgostoptekhisdat, Baku (in Russian).

421    Lazic, B., Kahlenberg, V., and Konzett, J. (2005) Rietveld analysis of a high pressure

422        modification of Monocalcium Oxogallate $(CaGa_2O_4)$, Zeitschift für Anorganische und

423        Allgemeine Chemie, 631, 2411-2415.

424

17

425   Lazic, B. Kahlenberg, V. Konzett, J., and Kaindl, R. (2006) On the polymorphism of $CaAl_2O_4$

426       - structural investigations of two high pressure modifications, Solid State Science, 8, 589-

427       597.

428   Lepicard, G. and Protas, J. (1966)  Etude structurale de l'oxyde double de manganese et de

429       calcium orthorhombique $CaMn_2O_4$ (marokite). Bulletin de la Societe Française de

430       Mineralogie et de Cristallographie,  89, 318-324.

431   Matthews, A. and Gross, S. (1980) Petrologic evolution of the Mottled Zone (Hatrurim)

432       metamorphic complex of Israel. Israel Journal of Earth Sciences, 29, 93-106.

433   Merlini, M., Hanfland, M., Gemmi, M., Huotari, S., Simonelli, L., and Strobel, P. (2010) $Fe^{3+}$

434       spin transition in $CaFe_2O_4$ at high pressure. American Mineralogist, 95, 200-203.

435   Minster, T., Yoffe, O., Nathan, Y., and Flexer, A. (1997) Geochemistry, mineralogy, and

436       paleoenvironments of deposition of the Oil Shale Member in the Negev. Israel Journal of

437       Earth Sciences, 46, 41-59.

438   Müller-Buschbaum, H. and von Schenk, R. (1970) Untersuchungen an $SrYb_2O_4$, $CaYb_2O_4$

439       und $CaLu_2O_4$: Ein Beitrag zur Kristallstruktur des Calciumferrat(III) Typs. Zeitschrift

440       fuer Anorganische und Allgemeine Chemie, 377, 70-78.

441   Niazi, A., Bud'ko, S.L., Schlagel, D.L., Yan, J.Q., Lograsso, T.A., Kreyssig, A., Das, S.,

442       Nandi, S., Goldman, A.I., Honecker, A., McCallum, R.W., Reehuis, M., Pieper, O., Lake,

443       B., and Johnston, D.C. ( 2009) Single-crystal growth, crystallography, magnetic

444       susceptibility, heat capacity and thermal expansion of the antiferromagnetic S=1 chain

445       compound $CaV_2O_4$. Physical Review, Serie 3. B - Condensed Matter, 79, 104432-1

446       104432-21.

447   Nigmatulina, E.N. and Nigmatulina, E.A. (2009) The pyrogenetic iron ores of the ancient coal

448       fires of Kuzbass. Zapiski Vsesoyuznogo Mineralogicheskogo Obshchestva, 1, 52-67.

18

449  Novikov, I., Vapnik. Ye., and Safonova, I. (2013) Mud Volcanism Origin of the Mottled

450      Zone, South Levant. Geoscience Frontiers (in print).

451  Pekov, I.V., Zelenski, M.E., Zubkova, N.V., Yapaskurt, V.O., Chukanov, N.V., Belakovskiy,

452      D.I., and Pushcharovsky, D. Yu (2012) Calciolangbeinite, $K_2Ca_2(SO_4)_3$, a new mineral

453      from the Tolbachik volcano, Kamchatka, Russia. Mineralogical Magazine, 76, 3, 673-

454      682.

455  Picard, L. (1931) Geological research in the Judean Desert. 108 p., Goldberg Press, Jerusalem.

456  Porat, N., Kolodny, Y., and Schwarcz, H.P. (1991) Timing of metamorphism in the Hatrurim

457      Basin - new evidence from ESR dating, Israel Geological Society Annual meeting 1991,

458      82.

459  Punin, Yu., O. and Franke, V.D. (2004) Curved-face growth of $NaNO_3$ crystals.

460      Crystallography Reports, 49, 256-260.

461  Rogge, M.P., Caldwell, J.H., Ingram, D.R., Green, C.E., Geselbracht, M.J., and Siegrist, T.

462      (1998) A new synthetic route to pseudo-brookite-type $CaTi_2O_4$. Journal of Solid State

463      Chemistry, 141, 338-342.

464  Salinas-Sánchez, A., García-Muñoz, J.L., Rodríguez-Carvajal, J., Sáez-Puche, R., and

465      Martínez, J.L. (1992) Structural characterization of $R_2BaCuO_5$ (R = Y, Lu, Yb, Tm, Er,

466      Ho, Dy, Gd, Eu and Sm) oxides by X-ray and neutron diffraction. Journal of Solid State

467      Chemistry, 100, 201–211.

468  Seryotkin, Yu.V., Sokol, E.V., and Kokh, S. (2012) Natural pseudowollastonite: Crystal

469      structure, associated minerals, and geological context. Lithos, 134-135, 75-90.

470  Sharygin, V.V., Lazic, B., Armbruster, T.M., Murashko, M.N., Wirth, R., Galuskina, I.O.,

471      Galuskin, E.V., Vapnik, Ye., Britvin, S.N., and Logvinova, A.M. (2013) Shulamitite

472      $Ca_3TiFe^{3+}AlO_8$ – a new perovskite-related mineral from Hatrurim Basin, Israel. European

473      Journal of Mineralogy, 25, 97–111.

19

474    Sheldrick, G. M. (2008) A short history of SHELX, Acta Crystallographica, A64, 112-122.

475    Shizuya, M., Isobe, M., and Takayama-Muromachi, E. (2007) Structure and properties of the

476      $CaFe_2O_4$-type cobalt oxide $CaCo_2O_4$. Journal of Solid State Chemistry, 180, 2550–2557.

477    Shnyukov, E.F., Slipchenko, B.V., and Kutniy, V.A. (1978) Produkty obzhiga sopochnikh

478      brekchiy (na gryazevych vulkanakh Azerbaidzana). In: Osadochnie porody i rudy, Materialy

479      nauchnich soobcheniy, 105-119 p. Naukova Dumka, Kiev (in Russian).

480    Sneh, A., Bartov, Y., Rosensaft, M., and Weissbort, T. (1998) Geological map of Israel

481      (1:200,000, sheets 1-4). Geological Survey of Israel.

482    Sokol, E.V., Gaskova, O.L., Kokh, S.N., Kozmenko, O.A., Seryotkin, Yu.V., Vapnik, Ye.,

483      and Murashko, M.N. (2011) Chromatite and its $Cr^{3+}$- and $Cr^{6+}$-bearing precursor minerals

484      from the Nabi Musa Mottled Zone complex, Judean Desert. American Mineralogist, 96,

485      659-674.

486    Sokol, E.V., Kozmenko, O.A., Kokh, S.N., and Vapnik, Ye. (2012) Gas reservoirs in the Dead

487      Sea area: evidence from chemistry of combustion metamorphic rocks in Nabi Musa fossil

488      mud volcano. Russian Geology and Geophysics 53, 745-762.

489    Sokol, E., Novikov, I., Zateeva, S., Vapnik, Ye., Shagam, R., and Kozmenko, O. (2010)

490      Combustion metamorphism in the Nabi Musa dome: new implications for a mud volcanic

491      origin of the Mottled Zone, Dead Sea area. Basin Research, 22 (4), 414-438.

492    Soudry, D., 1973. Bituminous rocks in the area of Nabi Musa. Geological Survey of Israel.

493      Report 541/73, 26 p. (in Hebrew).

494    Taylor, H.F.W. (1997) Cement chemistry. 2nd ed., 459 p. Thomas Telford Publishing,
495      London.

496    Vapnik, Ye. and Novikov, I.S. (2013) Reply to Comment of Y. Kolodny, A. Burg and A.

497      Sneh on "Combustion metamorphism in the Nabi Musa dome: new implications for a

498      mud volcano origin of the Mottled Zone, Dead Sea area", by E.Sokol, I. Novikov, S.

20

499      Zateeva, Ye. Vapnik, R. Shagam and O. Kozmenko, Basin Research (2010) 22, 414-438,

500      Basin Research 25, 115-120, doi: 10.1111/bre.12007.

501   Vapnik, Ye., Sharygin, V.V., Sokol, E.V., and Shagam, R**.** (2007)  Paralavas in a combustion

502      metamorphic complex: Hatrurim Basin, Israel. The Geological Society of American

503      Reviews in Engineering Geology, 18, 133-153.

504   Vapnik, Ye. and Sokol, E. (2006) Explosion breccias and diatremes as key structures in the

505      Formation of the Hatrurim Formation. Abstract in Bet-Shean, Israel Geological Society,

506      131.

507   Yamanaka, T., Komatsu, Y., Sugahara, M., and Nagai, T. (2005) Structure change of $MgSiO_3$,

508      $MgGeO_3$, and $MgTiO_3$ ilmenites under compression.  American Mineralogist, 90, 1301-

509      1307.

510   Yamanaka, T., Uchida, A., and Nakamoto, Y. (2008) Structural transition of post-spinel phases

511      $CaMn_2O_4$, $CaFe_2O_4$, and $CaTi_2O_4$ under high pressures up to 80 GPa. American

512      Mineralogist, 93, 1874–1881.

513   Yamaura, K., Huang, Q., Moldovan, M., Young, D.P., Sato, A., Baba, Y., Nagai, T., Matsui, Y.,

514      and Takayama Muromachi, E. ( 2005) High-pressure synthesis, crystal structure

515      determination, and a Ca substitution study of the metallic rhodium oxide $NaRh_2O_4$.

516      Chemistry of Materials, 17, 359-365.

517   Žaček, V., Skála, R., Chlupáčova, M., and Dvořák, Z. (2005) Ca-$Fe^{3+}$-rich, Si-undersaturated

518      buchite from Želénky, North-Bohemian Brown Coal Basin, Czech Republic. European

519      Journal of Mineralogy, 17, 623–633.

520

521

522

523

21

524

525

526

527 Figures captions

528 Fig. 1. Schematic geological map of the Judean Desert and eastern part of the Judean

529 mountains (modified after Sneh et al. 1998). The Hatrurim Complex: a - Nabi Musa; b - Jabel

530 Harmun; c - Hyrcania; d - Ma'ale Adummim.

531 Fig. 2. The eastern view of the Jabel Harmun. The rocks of the Hatrurim Complex overlay,

532 underlay and occur inside of the non-bituminous chalk belonging to the Ghareb Formation.

533 Fig. 3. Larnite-bearing nodules (pseudo-conglomerate) included into low-temperature matrix

534 composed of hydrated calcium silicates.

535 Fig. 4. A – Fragment of pseudo-conglomerate pebble, at the central part of which black ferrite

536 aggregates are visible. These aggregates are magnified in Fig. 3B; B – aggregate of two ferrite

537 grains: the smaller one of magnesioferrite-srebrodolskite composition, the larger one –

538 magnesioferrite prevailing at the margins (see Fig. 3A), central part is enriched in

539 srebrodolskite and harmunite; white and yellow selvedges of newly formed  sulphate hydrates

540 are well visible; C – skeletal intergrowth of parallel harmunite crystals; arrow shows the

541 prismatic crystal magnified in Fig. 3D; the same detail is shown in Fig. 3E, F; E – dark-grey

542 color of harmunite in reflected light; F – red internal reflections of harmunite visible in

543 reflected light with crossed polars.

544 A, B – optic images; C, D – back-scattered electrons (BSE) image; E, F – optic microscope,

545 reflected light, parallel and crossed polars, respectively.

546 Abbreviations of minerals used in Figs 4-8: Ag = native silver, Aph = aphtitalite, Brt = barite,

547 Clg = calciolangbeinite, Cu = native copper, Els = fluorellestadite, Hrm = harmunite, Hfr =

548 hydroferrite, Lrn = larnite, Mgf = magnesioferrite, Prv = perovskite, Shl = shulamitite, Srb =

549 srebrodolskite, Tnr = thenardite, Umg = umangite.

550 Fig. 5. A – general view of the rim of a black aggregation containing harmunite, sample not

551 rinsed by water; skeletal crystals of magnesioferrite and srebrodolskite are cemented by

552 calciolangbeinite, less frequent by aphthitalite and thenardite; B - octahedral crystal of

553 magnesioferrite with rounded faces and tops (anti-skeletal growth); C – twinned crystal of

554 native copper, umangite and native silver. Back-scattered electrons (BSE) image.

22

555    Fig. 6. Periphery of ferrite aggregation filled by calciolangbeinite with aphtitalite exsolution.

556    Magnified fluorellestadite crystal is shown in inset.

557    Fig. 7. A – BSE image of parallel intergrowth of harmunite, polished sample; B, C – reflected

558    light: B – light-grey color of harmunite under reflected light, C – red reflections of harmunite

559    in crossed polars.

560    Fig. 8. A - Replacement of harmunite after magnesioferrite. B – thin exolution-like structure

561    of harmunite in magnesioferrite.

562    High contrast BSE image, silicates are black.

563    Fig. 9. Raman spectra of harmunite. A – grain on Fig. 6A, B – exsolution-like lamellae in

564    magnesioferrite, Fig. 7A.

565    Fig. 10. (a) Crystal structure and (b) Ca-O bonds in the channels of $CaFe_2O_4$ (4 octahedra are

566    omitted for better visual representation).

567

568

23
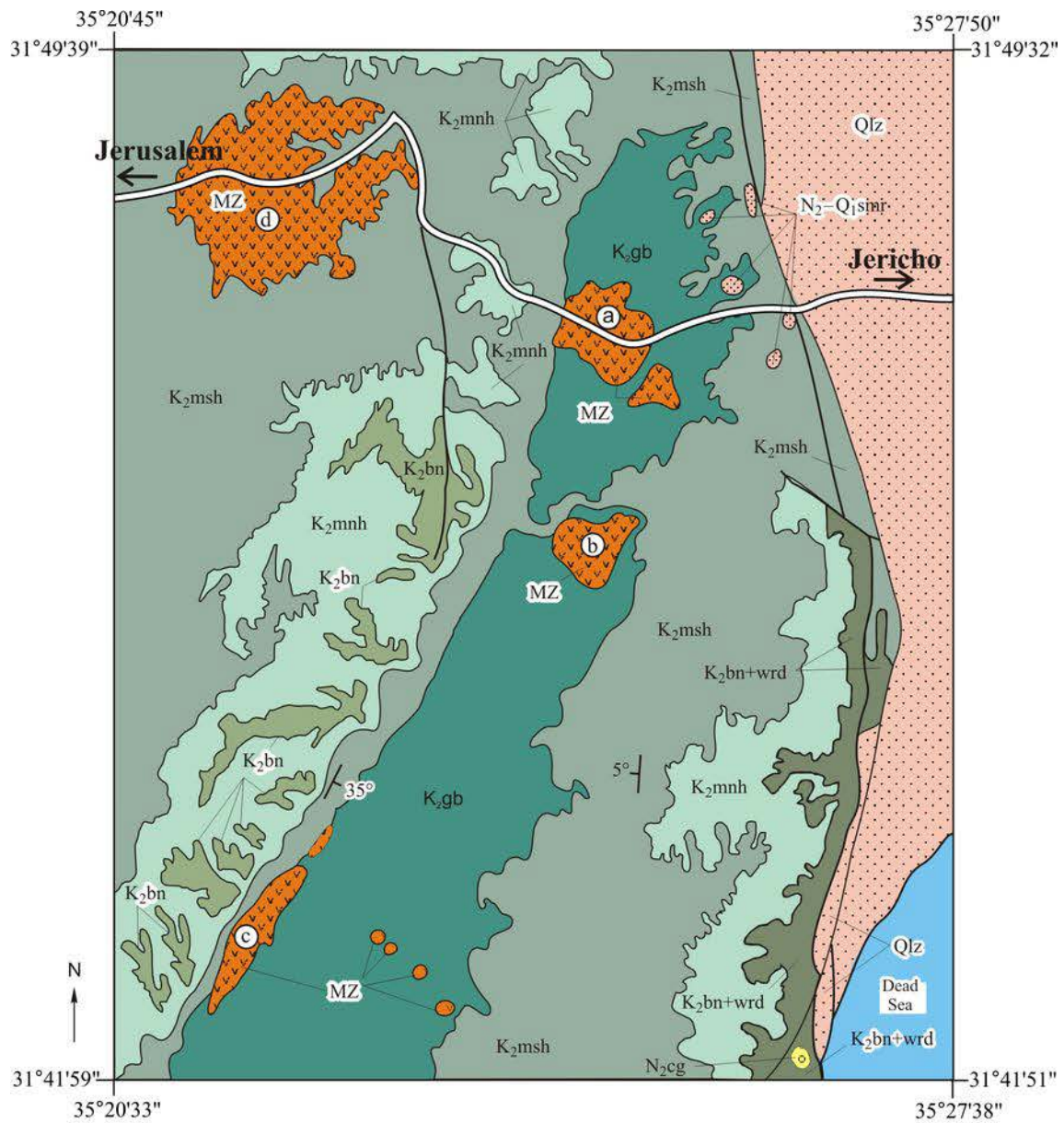
## LEGEND

| | |
|---|---|
| Qlz | Clay, silt, and sand, Lisan Fm, Pleistocene |
| N₂–Q₁smr | Sand, conglomerate, limestone, Samra Fm, Late Pliocene-Early Pleistocene |
| N₂cg | Conglomerate, Pliocene |
| K₂gb | Chalk, Ghareb Fm, Maastrichtian |
| K₂msh | Chert and phosphorite, Mishash Fm, Campanian |
| K₂mnh | Chalk, Menuha Fm, Santonian |
| K₂bn | Limestone, Bina Fm, Turonian |
| K₂wrd | Dolomite, Weradim Fm, Cenomanian |
| K₂bn+wrd | Undivided limestone, Bina and Weradim fms |
| MZ | Mottled Zone |
| | Fault |
| | Highway Jerusalem-Jericho |
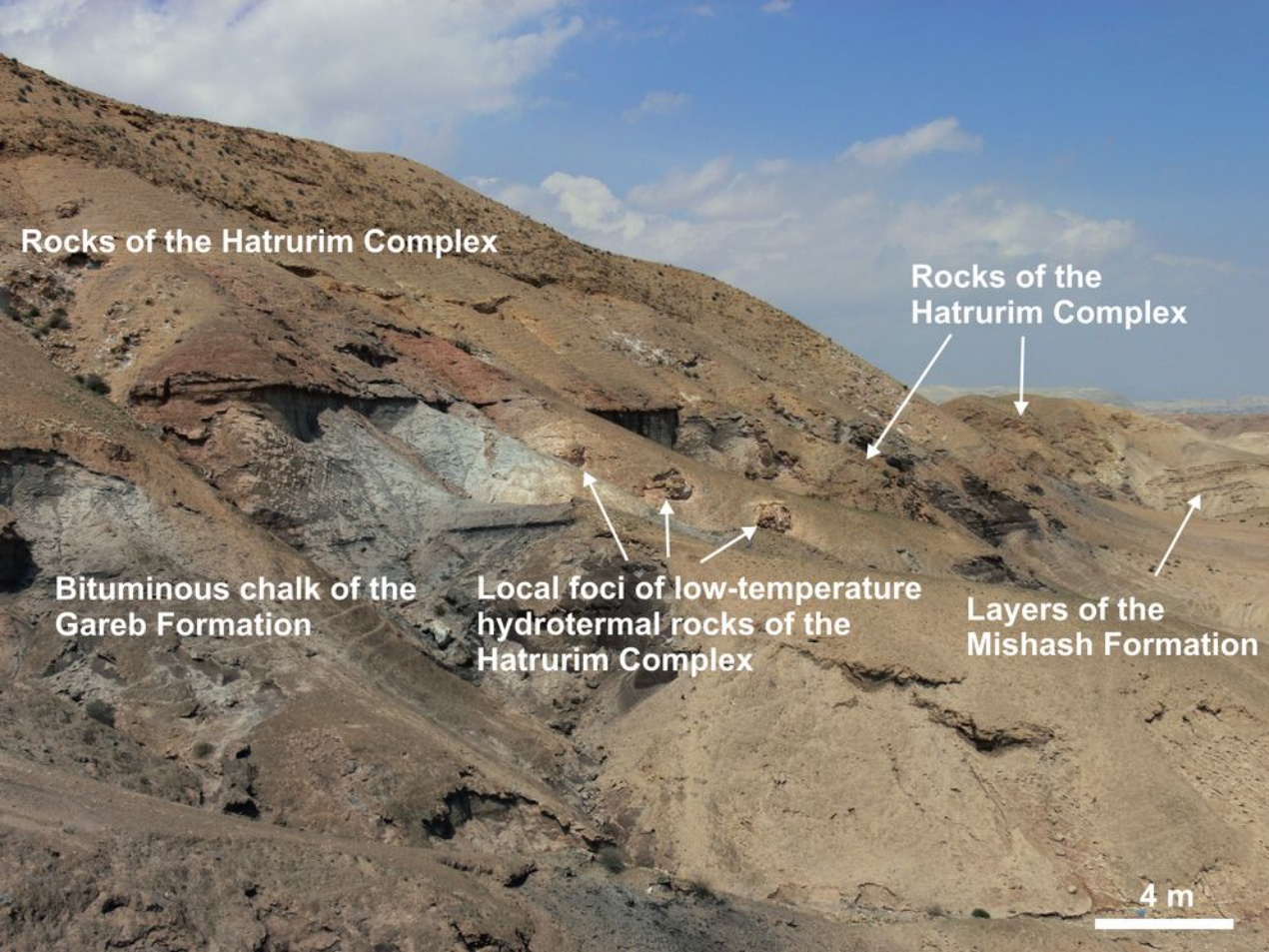
Rocks of the Hatrurim Complex

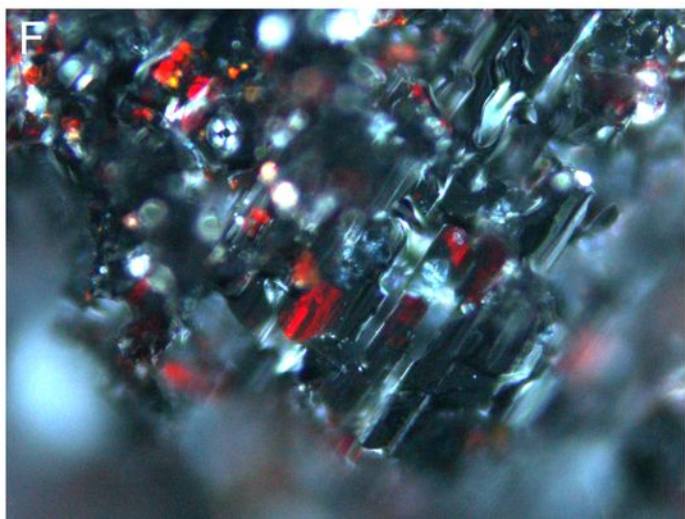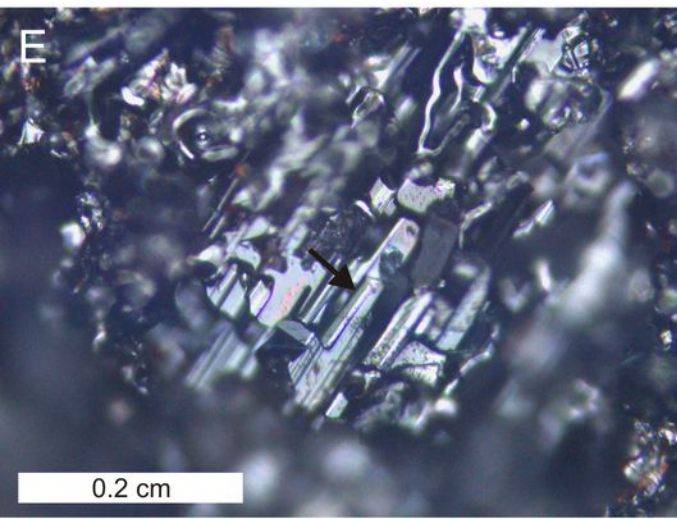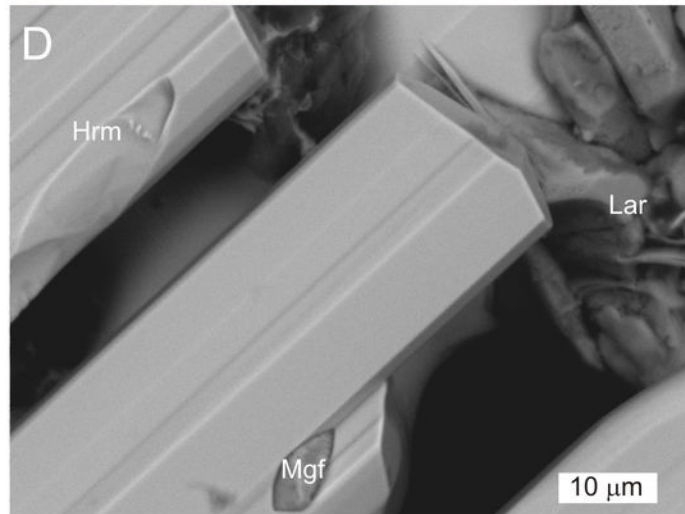Rocks of the Hatrurim Complex
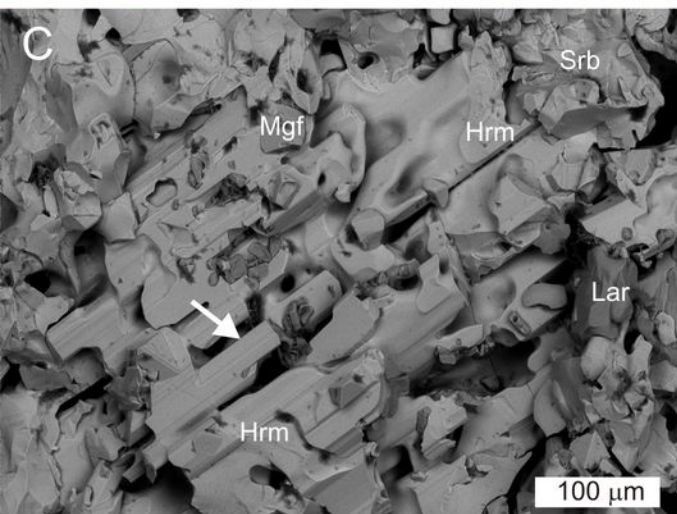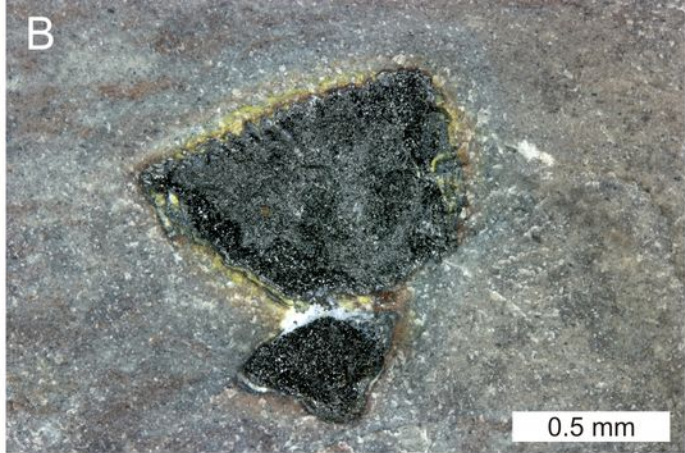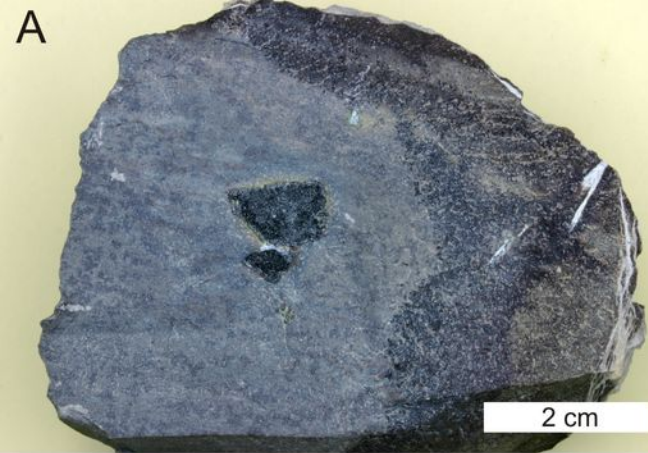
Bituminous chalk of the Gareb Formation

Local foci of low-temperature hydrotermal rocks of the Hatrurim Complex

Layers of the Mishash Formation
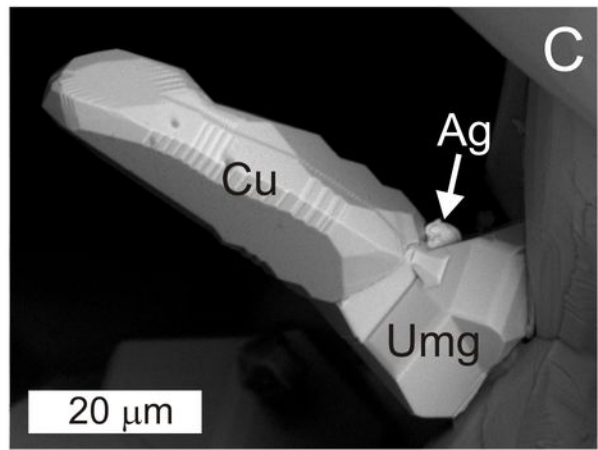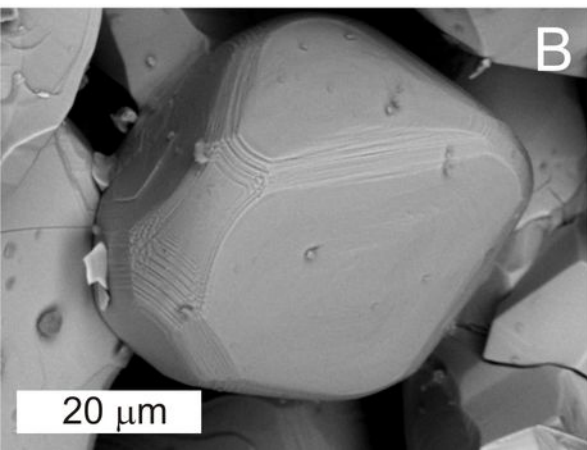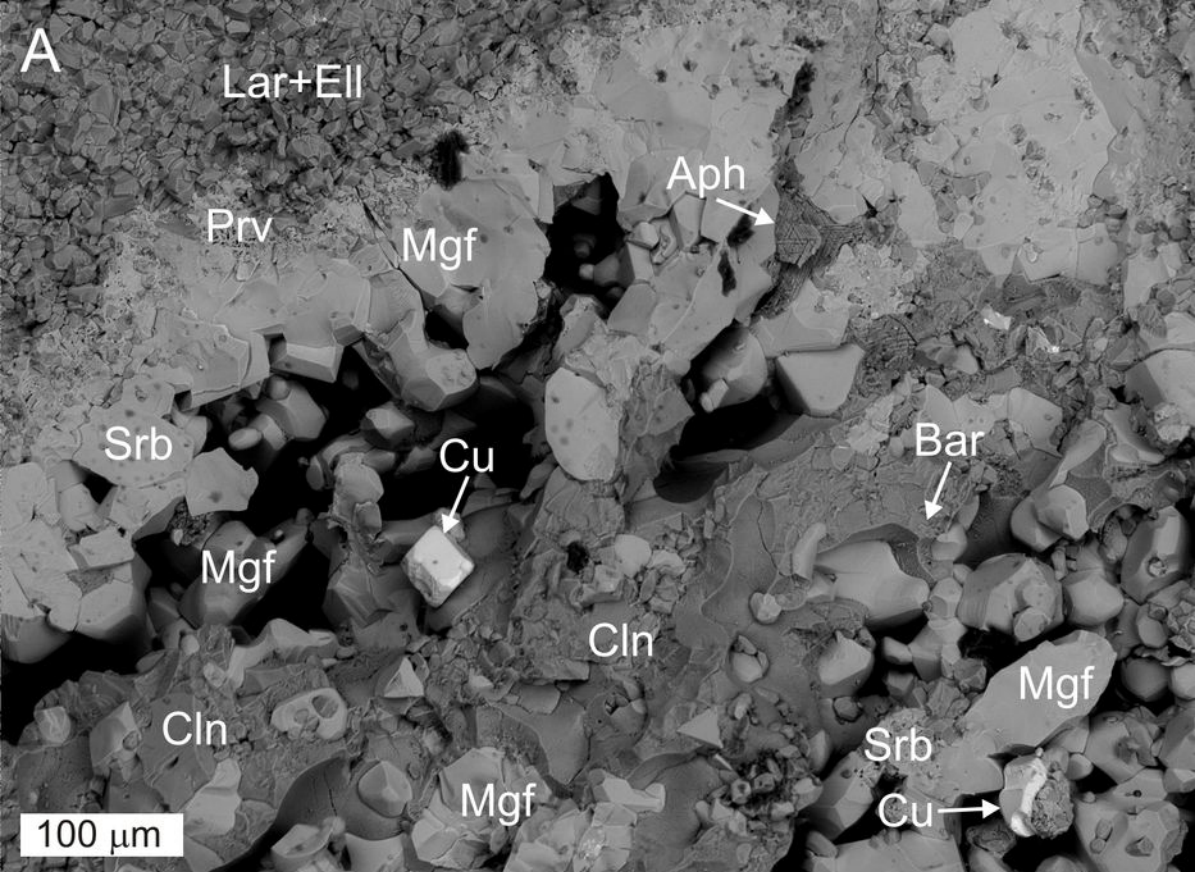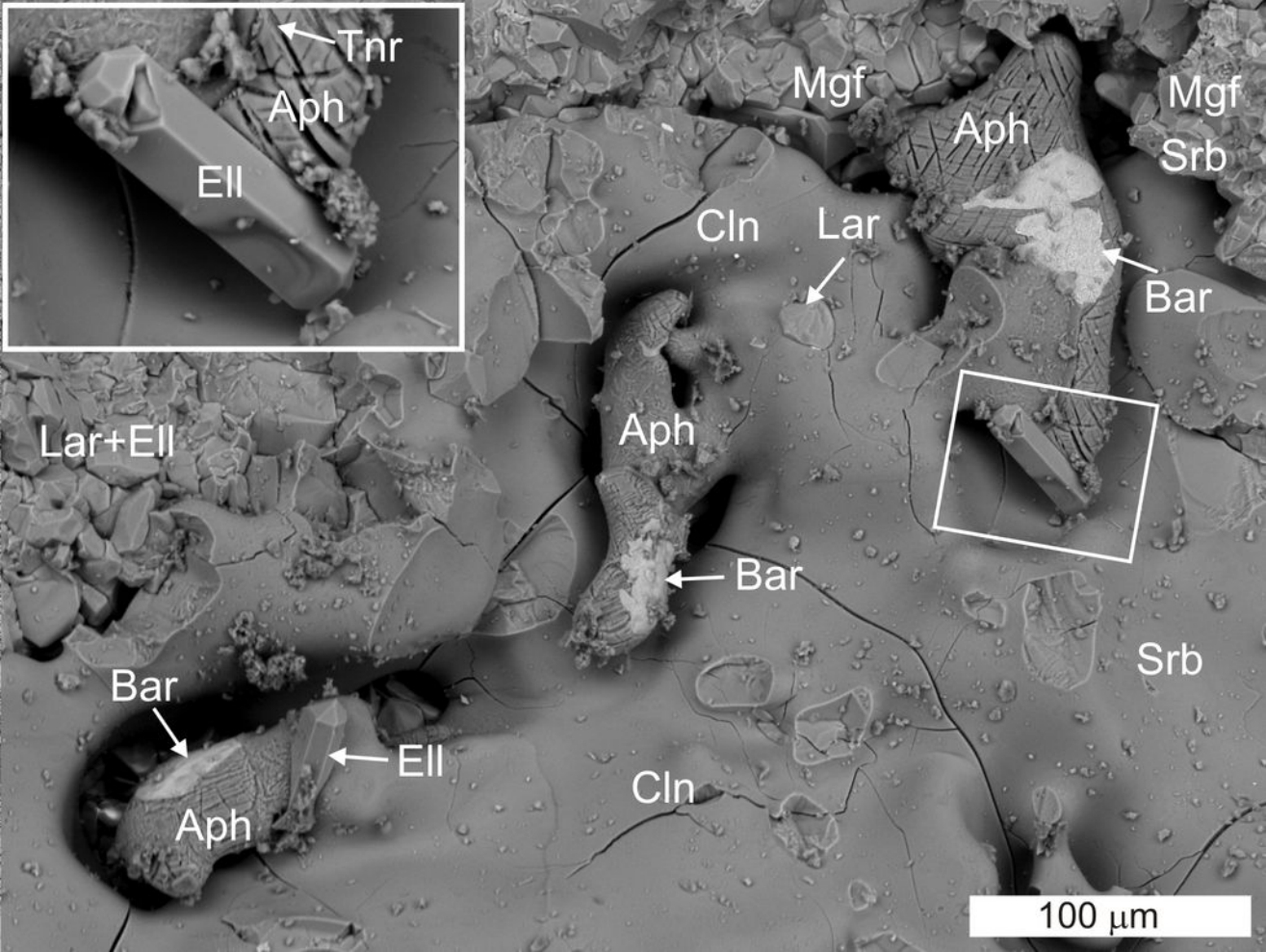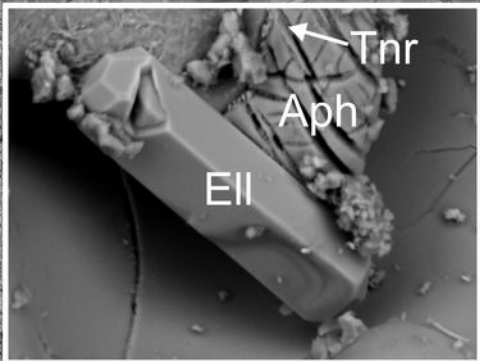
4 m
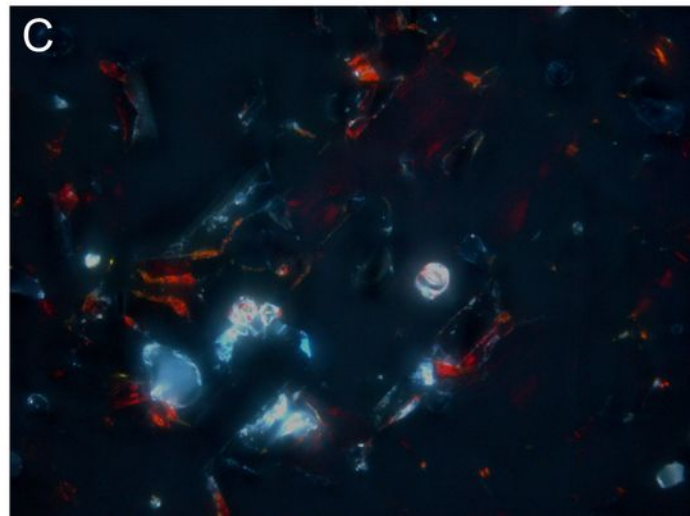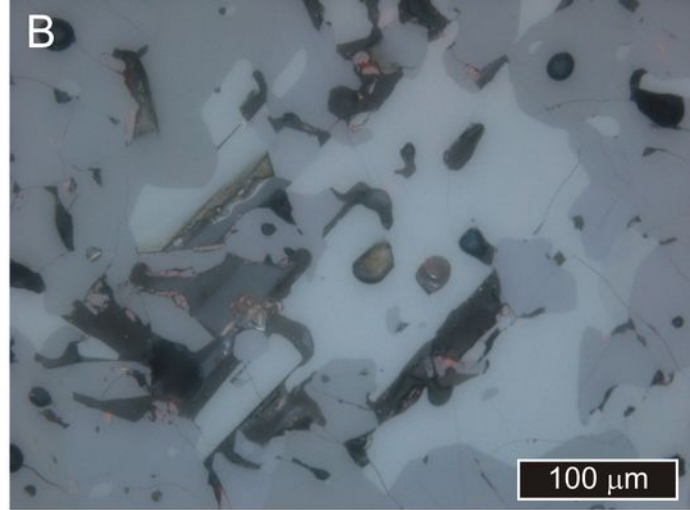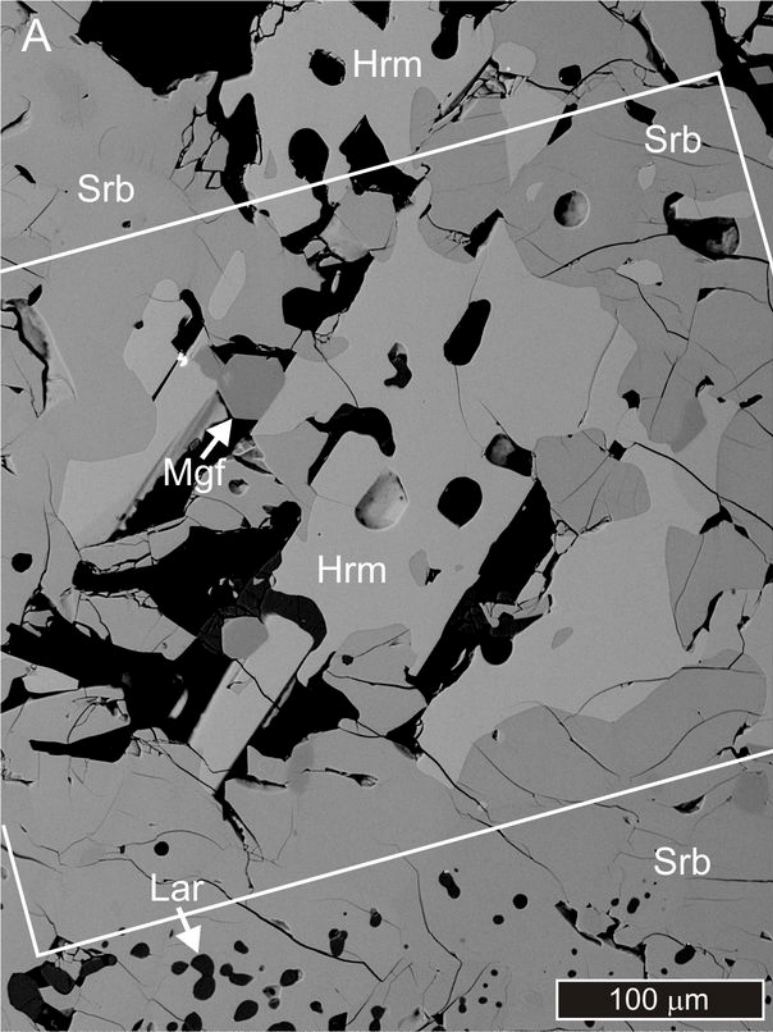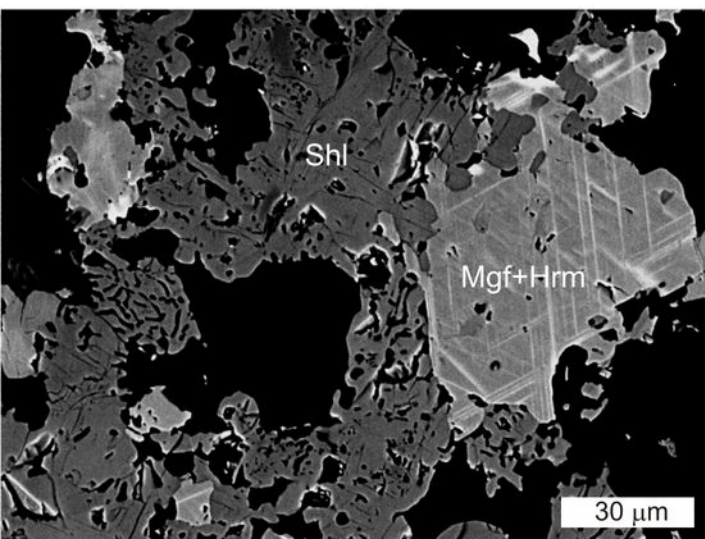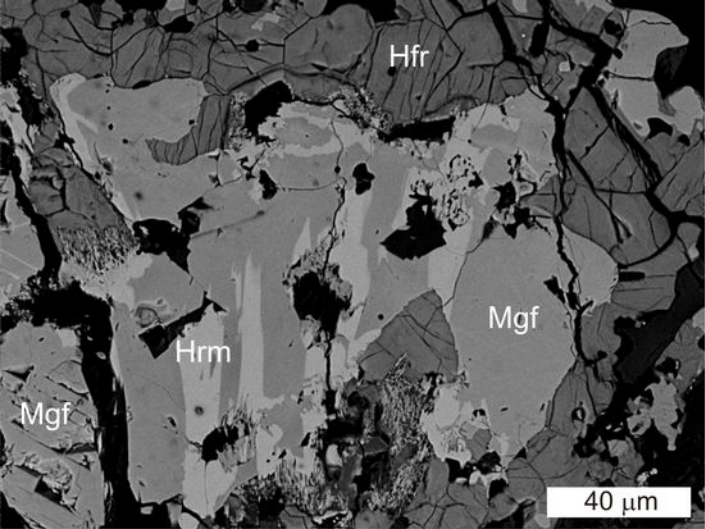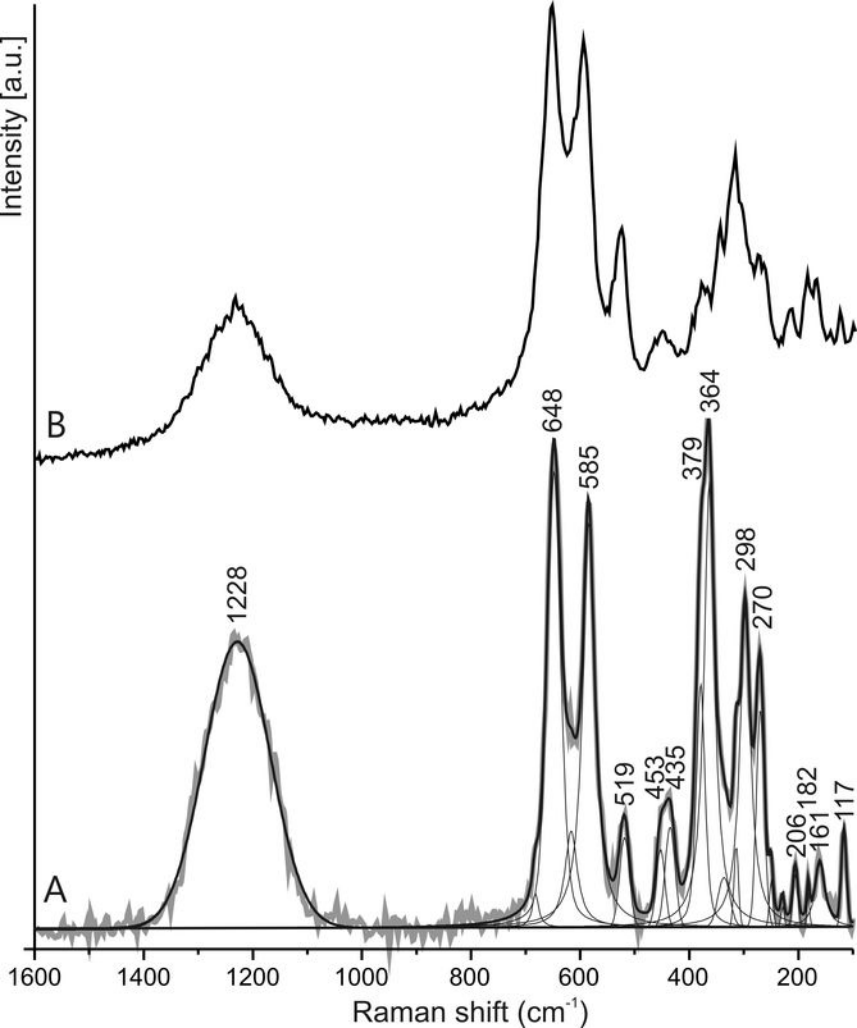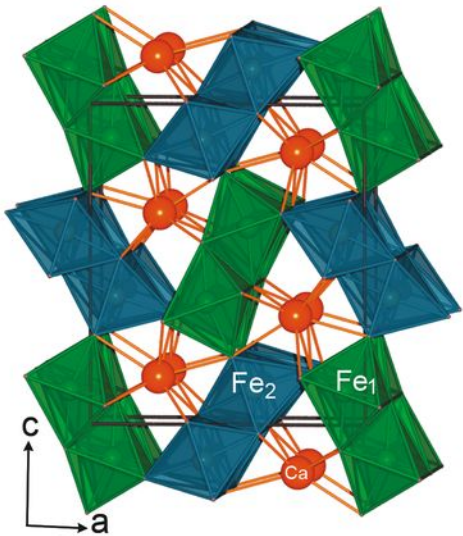
a
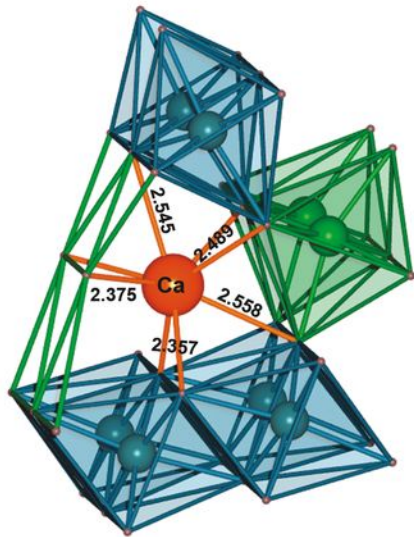
b

Table 1. Reflectance data (%) for harmunite.

| $R_{max}/R_{min}$ | λ/nm | $R_{max}/R_{min}$ | λ/nm |
|---|---|---|---|
| 22.20/20.10 | 400 | 20.05/18.95 | 560 |
| 22.90/19.90 | 420 | 19.70/18.65 | 580 |
| 22.30/20.10 | 440 | 19.30/18.45 | 589 (COM) |
| 22.00/20.25 | 460 | 19.30/18.35 | 600 |
| 21.60/20.10 | 470 (COM) | 19.00/18.00 | 620 |
| 21.40/20.00 | 480 | 18.80/17.80 | 640 |
| 21.30/19.70 | 500 | 18.70/17.75 | 650 (COM) |
| 21.20/19.55 | 520 | 18.30/17.50 | 660 |
| 20.80/19.25 | 540 | 18.30/17.35 | 680 |
| 20.65/19.20 | 546 (COM) | 18.10/17.15 | 700 |

Table 2. Composition of holotype harmunite (1), harmunite exsolutions in magnesioferrite (2), harmunite with maximum Cr content (3) and associated minerals: magnesioferrite (4) and srebrodolskite (5) from the Jebel Harmun.

| | 1 | | | 2 | | | 3 | 4 | 5 |
|---|---|---|---|---|---|---|---|---|---|
| | mean 13 | s.d. | range | mean 11 | s.d. | range | mean 2 | mean 9 | mean 5 |
| $SiO_2$ | | | | | | | | | 0.72 |
| $TiO_2$ | 0.15 | 0.08 | 0.07-0.31 | 0.13 | 0.2 | 0.02-0.75 | 0.02 | n.d. | 0.07 |
| $Fe_2O_3$* | 71.94 | 0.35 | 71.36-72.56 | 72.9 | 0.5 | 71.75-73.49 | 71.32 | 72.08 | 55.48 |
| FeO* | | | | | | | | 4.14 | 0.59 |
| $Cr_2O_3$ | 0.38 | 0.09 | 0.20-0.52 | 0.51 | 0.16 | 0.11-0.75 | 1.25 | 0.53 | 0.09 |
| $Al_2O_3$ | 0.36 | 0.07 | 0.26-0.45 | 0.71 | 0.16 | 0.50-1.00 | 0.83 | 3.36 | 0.65 |
| MnO | n.d. | | | 0.48 | 0.14 | 0.14-0.62 | 0.34 | 0.08 | n.d. |
| CaO | 26.15 | 0.14 | 25.80-26.31 | 25.92 | 0.29 | 25.31-26.42 | 25.71 | 1.26 | 41.42 |
| MgO | 0.06 | 0.02 | 0.04-0.09 | 0.06 | 0.03 | 0.03-0.15 | 0.08 | 15.82 | 0.02 |
| NiO | n.d | | | n.d | | | n.d | 0.86 | n.d. |
| ZnO | n.d | | | n.d | | | n.d | 0.56 | n.d. |
| CoO | n.d. | | | n.m. | | | n.m. | 0.11 | n.d. |
| $Na_2O$ | n.d. | | | 0.03 | 0.02 | 0.00-0.07 | 0.04 | n.d. | n.d. |
| Total | 99.04 | | | 100.74 | | | 99.59 | 99.51 | 99.05 |
| | | | | | | | | | |
| Ca | 1.013 | | | 0.986 | | | 0.988 | 0.046 | 2.011 |
| $Mn^{2+}$ | | | | 0.014 | | | 0.01 | 0.002 | |
| $Fe^{2+}$ | | | | | | | | 0.116 | |
| Mg | | | | | | | | 0.797 | |
| Na | | | | 0.002 | | | 0.003 | | |
| $Ni^{2+}$ | | | | | | | | 0.024 | |
| Co | | | | | | | | 0.003 | |
| Zn | | | | | | | | 0.012 | |
| **A** | **1.013** | | | **1.002** | | | **1.001** | **1.000** | **2.011** |
| $Fe^{3+}$ | 1.957 | | | 1.947 | | | 1.924 | 1.852 | 1.892 |
| $Ti^{4+}$ | 0.004 | | | 0.003 | | | 0.001 | | 0.002 |
| $Cr^{3+}$ | 0.011 | | | 0.014 | | | 0.036 | 0.014 | 0.003 |
| $Fe^{2+}$ | | | | | | | | | 0.023 |
| Mg | 0.003 | | | 0.003 | | | 0.004 | | 0.002 |
| Al | 0.015 | | | 0.03 | | | 0.035 | 0.134 | 0.035 |
| Si | | | | | | | | | 0.033 |
| **B** | **1.993** | | | **1.998** | | | **1.999** | **2.000** | **1.990** |

1-4 – calculated on 3 cations and 4O, 5 – calculated on 4 cations and 5O

* - FeO/$Fe_2O_3$ calculated on charge balance, s.d. – standard deviation, n.d. – not detected, n.m. – not measured

Table 3. X-ray powder diffraction data for harmunite.

| | | | observed | | calculated | | Decker and Kasper (1957) | |
|---|---|---|---|---|---|---|---|---|
| $h$ | $k$ | $l$ | $d_{obs}$ | $I_{rel}$ | $d_{calc}$ | $I_{calc}$ | $d_{obs}$ | $I_{rel}$ |
| 0 | 0 | 2 | 5.3393 | 2 | 5.3465 | 3 | | |
| 1 | 0 | 2 | 4.6203 | 5 | 4.6249 | 8 | | |
| 2 | 0 | 0 | 4.6090 | 13 | 4.6090 | 21 | 4.617 | 20 |
| 2 | 0 | 2 | 3.4889 | 6 | 3.4909 | 10 | 3.498 | 5 |
| 3 | 0 | 1 | 2.9529 | 2 | 2.9532 | 2 | | |
| 0 | 1 | 1 | 2.9007 | 4 | 2.9045 | 7 | | |
| 1 | 1 | 1 | 2.7669 | 3 | 2.7703 | 4 | | |
| **0** | **0** | **4** | **2.6697** | **52** | 2.6733 | 51 | 2.676 | 100 |
| **3** | **0** | **2** | **2.6632** | **100** | 2.6641 | 100 | | |
| 1 | 0 | 4 | 2.5643 | 2 | 2.5675 | 2 | | |
| **1** | **1** | **2** | **2.5244** | **60** | 2.5275 | 73 | 2.531 | 65 |
| **2** | **1** | **0** | **2.5225** | **35** | 2.5249 | 35 | | |
| 3 | 0 | 3 | 2.3260 | 1 | 2.3273 | 1 | | |
| 2 | 0 | 4 | 2.3101 | 1 | 2.3124 | 1 | | |
| 0 | 1 | 3 | 2.3002 | 4 | 2.3033 | 4 | | |
| 2 | 1 | 2 | 2.2808 | 3 | 2.2831 | 3 | | |
| 4 | 0 | 1 | 2.2527 | 3 | 2.2528 | 3 | | |
| **1** | **1** | **3** | **2.2318** | **34** | 2.2346 | 31 | 2.240 | 20 |
| 4 | 0 | 2 | 2.1159 | 10 | 2.1163 | 10 | 2.115 | 25 |
| 3 | 1 | 1 | 2.1093 | 17 | 2.1108 | 17 | | |
| 1 | 0 | 5 | 2.0806 | 3 | 2.0833 | 2 | | |
| 2 | 1 | 3 | 2.0581 | 3 | 2.0603 | 3 | | |
| 3 | 1 | 2 | 1.9957 | 4 | 1.9972 | 3 | | |
| 1 | 1 | 4 | 1.9531 | 13 | 1.9556 | 12 | 1.961 | 15 |
| 3 | 1 | 3 | 1.8414 | 8 | 1.8430 | 8 | | |
| **2** | **1** | **4** | **1.8335** | **40** | 1.8356 | 41 | 1.837 | 40 |
| **4** | **1** | **0** | **1.8307** | **27** | 1.8316 | 27 | | |
| 4 | 1 | 1 | 1.8044 | 13 | 1.8053 | 12 | 1.808 | 15 |
| 1 | 0 | 6 | 1.7475 | 2 | 1.7498 | 2 | | |
| 5 | 0 | 2 | 1.7427 | 3 | 1.7449 | 4 | | |
| 0 | 1 | 5 | 1.7426 | 4 | 1.7429 | 3 | 1.745 | 10 |
| 4 | 1 | 2 | 1.7317 | 3 | 1.7327 | 3 | | |
| 2 | 0 | 6 | 1.6603 | 14 | 1.6622 | 13 | 1.664 | 20 |
| 2 | 1 | 5 | 1.6300 | 1 | 1.6319 | 1 | | |
| 4 | 1 | 3 | 1.6280 | 2 | 1.6291 | 2 | | |
| 3 | 0 | 6 | 1.5401 | 16 | 1.5416 | 14 | 1.545 | 20 |
| 6 | 0 | 0 | 1.5364 | 12 | 1.5363 | 12 | 1.539 | 20 |
| 5 | 0 | 4 | 1.5170 | 2 | 1.5177 | 2 | | |
| 1 | 1 | 6 | 1.5118 | 18 | 1.5138 | 17 | | |
| **4** | **1** | **4** | **1.5098** | **19** | 1.5110 | 25 | 1.512 | 25 |
| 5 | 1 | 2 | 1.5086 | 17 | 1.5093 | 17 | | |
| 0 | 2 | 0 | 1.5070 | 19 | 1.5090 | 22 | | |
| 2 | 1 | 6 | 1.4543 | 11 | 1.4560 | 10 | 1.458 | 15 |
| 2 | 2 | 0 | 1.4324 | 1 | 1.4341 | 1 | | |
| 4 | 0 | 6 | 1.4086 | 2 | 1.4098 | 2 | 1.411 | 8 |
| 2 | 2 | 2 | 1.3835 | 1 | 1.3851 | 1 | | |
| 3 | 1 | 6 | 1.3714 | 2 | 1.3729 | 2 | 1.374 | 8 |
| 1 | 1 | 7 | 1.3465 | 2 | 1.3483 | 2 | | |
| 0 | 0 | 8 | 1.3348 | 2 | 1.3366 | 2 | | |
| 6 | 0 | 4 | 1.3316 | 11 | 1.3320 | 10 | 1.335 | 20 |

Table 4. Data collection and structure refinement details for harmunite.

| Crystal  data | Harmunite |
|---|---|
| Unit cell dimensions (Å) | $a = 9.2183(3)$ |
| | $b = 3.01750(10)$ |
| | $c =  10.6934(4)$ |
| | $\alpha = \beta = \gamma = 90°$ |
| Volume (Å$^3$) | 297.450(18) |
| Space group | *Pnma* |
| Z | 4 |
| Chemical formula | $CaFe_2O_4$ |
| | |
| *Intensity measurement* | |
| Crystal shape | prismatic |
| Crystal size (mm) | $0.05 \times 0.01 \times 0.01$ |
| | |
| Diffractometer | APEX II SMART |
| X-ray radiation | Mo$K\alpha$ $\lambda$ = 0.71073 Å |
| X-ray power | 50 kV, 30 mA |
| Monochromator | graphite |
| Temperature | 296 K |
| Time per frame | 30 s |
| Max. $\theta$ | 32.31 |
| Index ranges | $-13 \leq h \leq 13$ |
| | $-4 \leq k \leq 14$ |
| | $-15 \leq l \leq 16$ |
| No. of measured reflections | 6067 |
| No. of unique reflections | 623 |
| No. of observed reflections $(I > 2\sigma(I))$ | 483 |
| | |
| *Refinement of the structure* | |
| No. of parameters used in refinement | 44 |
| $R_{int}$ | 0.0629 |
| $R_\sigma$ | 0.0317 |
| $R1 , I > 2\sigma(I)$ | 0.0262 |
| $R1$ , all data | 0.0423 |
| w$R2$ (on $F^2$) | 0.0546 |
| GooF | 1.030 |
| $\Delta\rho_{min}$ (-e / Å$^3$) | -0.82 close to O3 |
| $\Delta\rho_{max}$ (e / Å$^3$) | 0.82 close to O2 |

Table 5. Final atom coordinates and anisotropic displacement parameters ($\text{Å}^2$) for harmunite.

| Atom | $x$ | $y$ | $z$ | $U_{iso}$ | $U_{11}$ | $U_{22}$ | $U_{33}$ | $U_{23}$ | $U_{13}$ | $U_{12}$ |
|------|-----|-----|-----|-----------|----------|----------|----------|----------|----------|----------|
| Ca1 | 0.75664(9) | -0.2500 | 0.34592(7) | 0.00828(18) | 0.0086(4) | 0.0073(4) | 0.0090(3) | 0 | -0.0004(3) | 0 |
| Fe1 | 0.56673(6) | 0.2500 | 0.61181(5) | 0.00735(15) | 0.0080(3) | 0.0070(3) | 0.0070(2) | 0 | -0.0002(2) | 0 |
| Fe2 | 0.08148(6) | -0.7500 | 0.39465(5) | 0.00754(16) | 0.0080(3) | 0.0068(3) | 0.0079(3) | 0 | 0.0004(2) | 0 |
| O1 | 0.5813(3) | 0.2500 | 0.4271(2) | 0.0078(6) | 0.0093(14) | 0.0077(14) | 0.0064(11) | 0 | -0.0018(10) | 0 |
| O2 | 0.8815(3) | -0.7500 | 0.4767(2) | 0.0078(6) | 0.0089(13) | 0.0063(13) | 0.0083(12) | 0 | 0.0013(10) | 0 |
| O3 | 0.7063(3) | -0.2500 | 0.6635(2) | 0.0079(5) | 0.0059(12) | 0.0084(14) | 0.0093(12) | 0 | 0.0015(10) | 0 |
| O4 | 0.4757(3) | 0.2500 | 0.7827(2) | 0.0073(5) | 0.0086(13) | 0.0076(13) | 0.0058(11) | 0 | 0.0019(9) | 0 |

Table 6. Selected interatomic distances (Å) and bond-valence sums (u.v.) for harmunite.

| Atom1 | Atom2 | distance (Å)/ bvs (v.u) |
|-------|-------|-------------------------|
| Ca1 | O2 | 2.358(2) ×2 |
| | O1 | 2.375(2) ×2 |
| | O3 | 2.489(2) ×2 |
| | O4 | 2.545(3) |
| | O4 | 2.558(3) |
| | average | 2.4438 |
| | bvs* | 2.259(5) |
| | | |
| Fe1 | O1 | 1.980(3) |
| | O4 | 2.011(3) |
| | O3 | 2.0583(19) ×2 |
| | O1 | 2.0767(18) ×2 |
| | average | 2.0435 |
| | bvs* | 2.795(6) |
| | | |
| Fe2 | O4 | 1.9969(17) ×2 |
| | O2 | 2.042(3) |
| | O3 | 2.053(3) |
| | O2 | 2.0699(18) ×2 |
| | average | 2.03798 |
| | bvs* | 2.832(6) |

* bvs - bond-valence sums (Brown and Altermatt 1985)

Table 7. Bond-valence sums (bvs) and global instability index (GII) calculated for diverse compounds with calcium-ferrite structure type and two slightly distorted modifications $CaTi_2O_4$-type (**CT**) and $CaMn_2O_4$-type (**CM**)

| Compounds with calcium ferrite structure | bvs of $Ca^{2+}/Mg^{2+}$ | bvs of (3+) cation in octahedra | GII | References for structural data |
|---|---|---|---|---|
| $CaFe_2O_4$ harmunite | 2.259( 5) | 2.832(6) / 2.795(6) | 0.15 | this paper |
| $CaMn_2O_4$ marokite | 2.263(10) | 2.886(14) | 0.16 | Lepicard and Protas 1966 |
| $FeCr_2O_4$ (meteorite) | | structural data not available | | Chen et al. 2008 |
| | | | | |
| Synthetic compounds (conditions of synthesis) | | | | |
| $CaSc_2O_4$ (2110 °C) | 1.879(28) | 2.895(48)/ 2.870(46) | 0.12 | Horyń and Lukaszewicz 1966 |
| $CaTi_2O_4$ (1000 °C) | 2.271(4) | 2.903(5)/1.989(2) | 0.13 | Rogge et al. 1998 |
| $CaV_2O_4$ (1200 °C) | 2.225( 16) | 2.735(21)/ 2.758(20) | 0.19 | Niazi et al. 2009 |
| $CaGa_2O_4$ (700 °C / 4 GPa) | 2.363(10) | 2.792(13)/ 2.827(12) | 0.19 | Lazic et al. 2005 |
| β - $CaCr_2O_4$ (1300 °C) | 2.371 | 2.769/2.847 | 0.19 | Hörkner and Müller-Buschbaum 1976 |
| $CaRh_2O_4$ (1500 °C / 6 GPa) | 2.308(4) | 3.252(6)/3.114(6) | 0.21 | Yamaura et al. 2005 |
| $CaYb_2O_4$ (2300 °C) | 1.661 | 2.678/ 2.942 | 0.24 | Müller-Buschbaum and von Schenk 1970 |
| $CaAl_2O_4$ (1100 °C / 10 GPa) | 2.595(6) | 2.520(7)/ 2.557(7) | 0.36 | Lazic et al. 2006 |
| $CaCo_2O_4$ (1500 °C / 6 GPa) | 2.793(16) | 2.535(14)/ 2.728(16) | 0.37 | Shizuya et al. 2007 |
| $MgAl_2O_4$ (2200 °C / 27 GPa) | 1.833( 11) | 2.690(19)/2.822(18) | 0.21 | Kojitani et al. 2007 |
| $CaTi_2O_4$ (1000 °C) | 2.271(4) | 2.903(5)/1.989(2) | 0.13 | Rogge et al. 1998 |
| $CaTi_2O_4$ (80 GPa) (CT) | 3.742(249)/ 3.734(329) | 4.341(390)/ 4.316(397) | 1.29 | Yamanaka et al. 2005 |
| $MgFe_2O_4$ (37.3 GPa) (CM) | 4.587(710) | 3.233(537) | 1.29 | Andrault and Bolfan Casanova 2001 |